Constraining Europa's subsolar atmosphere with a joint analysis of HST spectral images and Galileo magnetic field data

S. Cervantes [1], J. Saur [1]

[1]Institute of Geophysics and Meteorology, University of Cologne, Germany

Key Points:

- We combine HST spectral images and Galileo magnetometer data to constrain the density and location of water vapor in Europa's atmosphere
- We simulate the plasma interaction for Galileo E12 flyby with a three-component atmosphere: global O_2, stable and confined H_2O, and a plume
- Using 50% of the O_2 and H_2O column densities from Roth [2021] in our MHD model yields magnetic field signatures consistent with observations

Corresponding author: S. Cervantes, `jcervant@uni-koeln.de`

Abstract

We constrain Europa's tenuous atmosphere on the subsolar hemisphere by combining two sets of observations: oxygen emissions at 1304 Å and 1356 Å from Hubble Space Telescope (HST) spectral images, and Galileo magnetic field measurements from its closest encounter, the E12 flyby. We describe Europa's atmosphere with three neutral gas species: global molecular (O_2) and atomic oxygen (O), and localized water (H_2O) present as a near-equatorial plume and as a stable distribution concentrated around the subsolar point on the moon's trailing hemisphere. Our combined modelling based on the ratio of OI 1356 Å to OI 1304 Å emissions from Roth (2021) and on magnetic field data allows us to derive constraints on the density and location of O_2 and H_2O in Europa's atmosphere. We demonstrate that 50% of the O_2 and H_2O abundances from Roth (2021) are required to jointly explain both the HST and Galileo measurements. The column densities of 1.24×10^{18} m^{-2} and 1.47×10^{19} m^{-2} for O_2 and H_2O, respectively, derived by our analysis however still lie within the uncertainties of Roth (2021). Our results provide additional evidence for the existence of a stable H_2O atmosphere at Europa.

1 Introduction

Europa is thought to harbor a global liquid water (H_2O) ocean under its icy surface (Carr et al., 1998; Khurana et al., 1998; Kivelson et al., 2000), and is therefore a prominent candidate in the search for extraterrestrial life. Previous observations of water vapor in the form of transient plumes rising above Europa's surface (Roth et al., 2014) might carry the possibility to probe the ocean water above the surface, and the upcoming ESA's JUICE (Grasset et al., 2013) and NASA's Europa Clipper missions (Howell & Pappalardo, 2020) have initiated further interest to better understand this moon's atmosphere, its interior, and its plasma environment.

Molecular oxygen (O_2) was the first constituent to be detected in Europa's atmosphere (Hall et al., 1995), but a stable H_2O component, in contrast to the sporadic plumes, remained undetected for a long time. Roth (2021) analyzed a set of Hubble Space Telescope (HST) spectral images, and provided the first evidence of a persistent H_2O distribution in the central sunlit trailing hemisphere of the moon. This same region was traversed by the Galileo spacecraft in 1997 along its E12 flyby, and the magnetometer on board measured the magnetic field as the spacecraft approached the moon on its closest encounter.

The primary means of detecting Europa's neutral gas environment is via emission of its atomic constituents. Hall et al. (1995) performed the first observations of the moon's atmosphere using HST observations, and the ultraviolet (UV) spectrum revealed emissions at 1304 Å and 1356 Å. The ratio of atomic oxygen emission at these two wavelengths, r_γ = OI 1356 Å/OI 1304 Å, yielded a value of 1.9, which implied electron impact dissociative excitation of O_2 as the emission process. Later studies (e.g. Hall et al., 1998; Roth et al., 2016) presented additional sets of HST UV images of Europa's atmosphere, and their measured ratios r_γ were consistently larger than 1. These results supported the conclusion that Europa's atmosphere is dominated by O_2. Years later, Roth et al. (2014) reported surpluses of hydrogen Lyman-α and OI 1304 Å emissions near Europa's south pole from HST images. Their results were interpreted as a local atmospheric inhomogeneity, consistent with an active water plume as a source. The lack of detection of these emissions in other observations suggested varying plume activity of intermittent nature.

Recently, Roth (2021) inspected the radial profile of the oxygen emission ratio r_γ for several HST observations at different orbital locations of Europa. A major finding was that for the trailing side visits, r_γ systematically decreased from the limb towards the disk center. This profile was shown to be in agreement with an H_2O-dominated atmosphere concentrated around the subsolar point, and an O_2-dominated atmosphere elsewhere. Furthermore, the reduced oxygen emission ratio on the disk center was found to be consistent within uncertainties among the four trailing side visits, obtained between 1999 and 2015. However, the source of this persistent H_2O atmosphere could not be unambiguously identified, as the values calculated by Roth (2021) are approximately two orders of magnitude larger than the predicted H_2O column densities for sputtering and sublimation of water ice at Europa's surface temperature (Shematovich et al., 2005; Smyth & Marconi, 2006; Plainaki et al., 2013; Vorburger & Wurz, 2018).

In addition to observations of Europa's neutral environment at different wavelengths, several models have been developed to describe the moon's atmosphere and to better constrain its generation process. Shematovich et al. (2005) and Smyth and Marconi (2006) used a Monte Carlo (MC) technique for the water group species to determine the atmospheric compositional structure and gas escape rates. Plainaki et al. (2010) and Plainaki et al. (2012) performed an MC calculation for the generation of Europa's atmosphere and incorporated sputtering information from laboratory measurements. Teolis et al. (2017) also implemented an MC model, and assumed a water plume source with multiple organic and nitrile species, in addition to sputtering, radiolysis, and other surface processes. Vorburger and Wurz (2018) modelled the formation of Europa's atmosphere via an MC code and considered sputtering by ions and electrons, as well as sublimation for some species.

Europa orbits Jupiter at the outer edge of the inner magnetosphere and is constantly overtaken by the corotating Jovian plasma. Close to the moon, ionization and collisions within Europa's atmosphere modify the plasma flow around it and generate magnetic field perturbations. Over eight close flybys between 1996 and 2000, the instruments on board Galileo measured local field and plasma perturbations, and hence provided a tool to probe Europa's neutral gas environment. Various numerical simulations following different approaches have been performed in order to match the spacecraft observations and to understand the plasma interaction with Europa and its atmosphere. Such models range from two-fluid codes (e.g. Saur et al., 1998), to single-fluid magnetohydrodynamic (MHD) (e.g. Kabin et al., 1999; Schilling et al., 2007, 2008; Blöcker et al., 2016) and multi-fluid MHD models (e.g. Rubin et al., 2015; Harris et al., 2021), and hybrid codes (e.g. Arnold et al., 2019, 2020). These numerical simulations have been employed to estimate plasma production and neutral loss rates, constrain the atmosphere distribution, explore the properties of a subsurface ocean, and study the effect of localized water plumes.

In this work, we present a parametrization of Europa's subsolar atmosphere and provide constraints on the column densities and location of the neutral O_2 and H_2O by combining two datasets: (a) the observed profile of the oxygen emission ratio from HST spectral images by Roth (2021), and (b) magnetic field measurements collected by the Galileo magnetometer (MAG) for its E12 flyby. First, we vary the abundances of O_2, O, and H_2O calculated by Roth (2021) to derive several possible distributions that fit the emission ratio profile, all within the uncertainties of the observations. Next, we use these distributions in a three-dimensional MHD code and simulate Europa's interaction with the Jovian plasma. These results allow us to identify the densities that are the most consistent both with the HST and MAG data. Finally, we consider uncertainties in certain parameters of the atmospheric and MHD model and assess the robustness of our results.

This paper is organized as follows: in section 2, we present the neutral atmosphere model and compute the emission intensities, and in section 3 we describe the single-fluid MHD model for the plasma interaction. In Section 4, we present our derived oxygen emission ratio profiles for several assumed neutral gas distributions, and we show the respective MHD simulations. In section 5, we perform a parameter study for different H_2O and electron properties, and we also discuss our findings with respect to the plasma environment and Europa's neutral atmosphere. Finally, Section 6 summarizes the most important results.

2 Atmosphere Model and Emission Rates

We assume a model of Europa's neutral atmosphere consisting of three species: O_2, O, and H_2O, and we simulate the respective electron-excited oxygen emissions. The goal is to reproduce the observed radial profile of the oxygen emission ratio from Roth (2021) using a simplified description with as few parameters as possible.

2.1 Atmosphere Model

For the three neutral gas species, we consider exponentially decreasing radial distributions with the column densities estimated by Roth (2021). The O_2 distribution is considered global as this molecule does not stick to the surface, as H_2O does, or thermally escape Europa's gravity, as H_2 does (Johnson et al., 2009; McGrath et al., 2009; Plainaki et al., 2018). Therefore, it is the dominant species in Europa's atmosphere (Hall et al., 1995), and it accumulates approximately uniformly over the moon (McGrath et al., 2009; Bagenal & Dols, 2020). Previous modelling studies (e.g. Saur et al., 1998; Schilling et al., 2007; Jia et al., 2018; Arnold et al., 2019) have considered an upstream-downstream asymmetry in the O_2 atmosphere. However, in this work we deliberately omit this asymmetry and keep the O_2 distribution as simple as possible in order to better demonstrate the effects of the localized H_2O on the plasma interaction. The scale height of the global O_2 is fixed to 150 km, as considered in previous modelling studies (e.g. Saur et al., 1998; Schilling et al., 2007), and similar to the best fit OI 1356 Å scale height from Roth et al. (2016). With an O_2 column density of $N_{O_2} = 2.47 \times 10^{18}$ m^{-2}, we get a surface number density of $n_{O_2,0} = 1.64 \times 10^{13}$ m^{-3}. The number density of the radially symmetric O_2 is given by:

$$n_{O_2}(h) = n_{O_2,0} \exp\left(-\frac{h}{H_{O_2}}\right), \tag{1}$$

with scale height H_{O_2} and altitude $h = r - R_E$ above the surface, with Europa's radius $R_E = 1569$ km.

As a second constituent, we consider atomic O produced through the dissociation of the molecular oxygen. Similar to O_2, the abundance of O is also described by an exponential decrease. In line with Roth et al. (2016), we assume a 2 times larger scale height for the lighter atomic O, i.e., $H_O = 300$ km. With the derived upper limit for the O abundance from Roth (2021), equal to 6×10^{16} m^{-2}, the surface number density of atomic O is $n_{O,0} = 2 \times 10^{11}$ m^{-3}. It must be emphasized that while atomic O is included in our atmospheric model to reproduce the observed profile of the oxygen emission ratio, it is not taken into account in the MHD modelling (Section 3), as the maximum O/O_2 mixing ratio of 0.03 (Roth, 2021) deems it too dilute to impact the plasma interaction.

In accordance with the results of Roth (2021), we assume an H_2O distribution strongly concentrated around the subsolar point in the trailing hemisphere, described by the following equation:

$$n_{H_2O}(h, \alpha) = n_{H_2O,0} \cos^{\beta}(\alpha) \exp\left(-\frac{h}{H_{H_2O}}\right), \tag{2}$$

where α is the angle to the subsolar point. H_2O freezes on contact with the icy surface, limiting its abundance in the atmosphere. Hence, the exponent β is introduced in equation (2) to restrict the spatial distribution. The resulting H_2O atmosphere is highly localized with a maximum at the subsolar point and is frozen on the nightside of Europa.

The maximum dayside temperature at Europa's surface is 132 K (Spencer et al., 1999), and therefore we assume an H_2O scale height of 46 km. The column density is

$N_{\mathrm{H_2O}} = 2.95 \times 10^{19}$ m^{-2} (Roth, 2021), which results in a surface number density of $n_{\mathrm{H_2O},0} = 6.41 \times 10^{14}$ m^{-3}. The subsolar point is located at a longitude of 217.5° W (between the anti-Jovian meridian and the trailing hemisphere apex) and a latitude of 1° N as extracted from the Solar System SPICE kernel.

In addition, Jia et al. (2018) has provided in-situ evidence of a water plume on Europa from the magnetic field and plasma wave observations for the Galileo E12 flyby. Therefore, we also include the effect of a plume on the plasma interaction, and incorporate in our atmospheric model an analytical form for the density profile of the plume. We use the following description similar to Blöcker et al. (2016), Jia et al. (2018), and Arnold et al. (2019):

$$n_{\mathrm{pl}}(h, \tilde{\theta}) = n_{\mathrm{pl},0} \cdot \exp\left[-\left(\frac{h}{H_{\mathrm{pl}}}\right) - \left(\frac{\tilde{\theta}}{H_\theta}\right)^2 \right], \tag{3}$$

where $n_{\mathrm{pl},0}$ is the surface number density of the neutral gas in the center of the plume, H_{pl} is the scale height, $\tilde{\theta}$ is the angular distance from the center of the plume, and H_θ is the opening angle. The numerical values used are: $n_{\mathrm{pl},0} = 3 \times 10^{15}$ m^{-3}, $H_{\mathrm{pl}} = 150$ km, and $H_\theta = 3^o$. The angular distance measured relative to the central axis of the plume $\tilde{\theta}(\theta, \phi)$ is given by:

$$\tilde{\theta}(\theta, \phi) = \arccos\left[\sin(\theta)\sin(\theta_{\mathrm{ap}})\cos(\phi - \phi_{\mathrm{ap}}) + \cos(\theta)\cos(\theta_{\mathrm{ap}})\right]. \tag{4}$$

with the spherical coordinates of the plume center θ_{ap} and ϕ_{ap}. Similar to Jia et al. (2018), the base of the plume is located at 245° W and 5° S. In addition, the plume is tilted with respect to the radial direction by 15° towards the east and 25° towards the south.

2.2 Emission Rates

We compute the emission rates produced by electron impact excitation of Europa's neutral atmosphere at two specific wavelengths: 1304 Å and 1356 Å. We assume a thermal electron population of 20 eV (Sittler & Strobel, 1987) plus a 250 eV suprathermal population (Johnson et al., 2009) with a 5% mixing ratio (Bagenal et al., 2015). In accordance with Roth (2021), we consider an electron density of 160 cm^{-3}. The collisional excitation rates $f_{n,\lambda}(T_e)$ at a wavelength λ are given as an integral over the Maxwell-Boltzmann distribution f_{Max}, the electron velocity $v(E)$, and the energy-dependent cross sections $\sigma_{n,\lambda}(E)$ for the collisions between the exciting electrons and the neutral species n according to:

$$f_{n,\lambda}(T_e) = \int_{E_t}^{\infty} f_{\mathrm{Max}}(E, T_e)\ \sigma_{n,\lambda}(E)\ v(E)\ \mathrm{d}E, \tag{5}$$

where E_t is the energy of the excitation threshold. For our computation of the emission rates, we set E_t to 14 eV as in Hartkorn et al. (2017). The electron impact excitation cross sections are based on the laboratory measurements of OI 1304 Å and OI 1356 Å emission intensities by Doering and Gulcicek (1989), Kanik et al. (2001), Kanik et al. (2003), and Makarov et al. (2004). The local volume emission rates $i_{n,\lambda}$ are, in turn, calculated by multiplying the density of the neutral atmospheric gas with the density of the impinging electrons and the emission rates. The intensity I_λ at a specific wavelength λ is then computed by integrating the local intensities over the line of sight.

We additionally calculate average intensities across the images in 0.025 R_E concentric rings around the disk center for both wavelengths, as follows:

$$I_\lambda = \int_{r_1}^{r_2} \mathrm{d}a \int_{\mathrm{los}} \frac{\sum_n i_{n,\lambda}}{10^{10}\ \pi\,(r_2^2 - r_1^2)}\ \mathrm{d}s, \tag{6}$$

where the intensity is given in Rayleigh; and r_1 and r_2 are the radii of the inner and outer circles limiting a concentric ring, respectively. Finally, the radial profile of the oxygen emission ratio r_γ is obtained by dividing the averaged OI 1356 Å intensity by the averaged OI 1304 Å intensity in all pixels within the respective concentric rings, similar to Roth (2021).

3 MHD Plasma Model

In order to describe the plasma interaction with Europa's atmosphere, we apply a three-dimensional single-fluid MHD model. Our simulations self-consistently calculate the magnetic field and bulk plasma properties. With the model results, we constrain the H_2O atmosphere by comparing observed and modelled magnetic field perturbations near Europa.

3.1 Geometry and Model Equations

We use a Cartesian and a spherical coordinate system, both with their origin in the center of the moon. The Cartesian system is the EPhiO system where the x axis points along the direction of the corotational plasma flow, the y axis corresponds to the Jupiter-Europa vector, and the z axis is parallel to Jupiter's spin axis. The spherical coordinate system is characterized by the radius r, the colatitude θ measured from the positive z axis, and the longitude ϕ measured from the positive y axis towards the negative x axis.

Our single-fluid MHD model consists of one evolution equation for each of the following four plasma variables: magnetic field $\mathbf{B}$, plasma bulk velocity $\mathbf{v}$, plasma mass density ρ, and internal energy density e. The equations read:

$$\frac{\partial \rho}{\partial t} + \nabla \cdot (\rho \mathbf{v}) = (P - L)\, m_i, \tag{7}$$

$$\frac{\partial \mathbf{v}}{\partial t} + (\mathbf{v} \cdot \nabla)\, \mathbf{v} = -\frac{1}{\rho} \nabla p + \frac{1}{\rho \mu_0} (\nabla \times \mathbf{B}) \times \mathbf{B} - \left(P \frac{m_i}{\rho} + \nu_n \right) \mathbf{v}, \tag{8}$$

$$\frac{\partial \mathbf{B}}{\partial t} = \nabla \times (\mathbf{v} \times \mathbf{B}), \tag{9}$$

$$\frac{\partial}{\partial t}\left(\frac{e}{\rho}\right) + (\mathbf{v} \cdot \nabla)\, \frac{e}{\rho} = -\frac{p}{\rho} \nabla \cdot \mathbf{v} + \frac{1}{2} v^2 \left(\frac{P m_i}{\rho} + \nu_n \right) - e \left(\frac{L m_i}{\rho^2} + \frac{\nu_n}{\rho} \right), \tag{10}$$

with ion mass m_i, plasma production and loss rates P and L, respectively, vacuum permeability μ_0, ion-neutral collision frequency ν_n, and plasma thermal pressure p, which is related to the internal energy density through $e = \frac{3}{2} p$. The plasma production and loss rates and the collision frequency specify various physical processes and their quantitative expressions are provided in the next section.

For the upstream magnetospheric plasma we use an average ion mass $\tilde{m}_i = 18.5$ amu and an effective ion charge $z_c = 1.5$ (Kivelson et al., 2004), as in previous studies of the Europa-plasma interaction (e.g. Blöcker et al., 2016; Arnold et al., 2019, 2020). The upstream plasma mass density can be written as: $\rho_0 = \tilde{m}_i n_e / z_c$ with the electron number density n_e. Finally, the upstream internal energy density is given by: $e_0 = \frac{3}{2} n_0 k_B (T_e + T_i)$ with the background ion density $n_0 = \rho_0 / \tilde{m}_i$.

Our upstream magnetospheric parameters are similar to those of Jia et al. (2018), who also modelled the plasma interaction around Europa for the Galileo flyby E12. We consider a bulk velocity of 100 km s^{-1} in the corotation direction. The Jovian background magnetic field is determined by excluding the perturbed values of the Galileo magnetometer data around 10 min of closest approach, performing a linear fit, and then extracting the fitted magnetic field values at closest approach, which results in $\mathbf{B}_0 = (78, 0, -395)$ nT. Based on Galileo's Plasma Wave Spectrometer (PWS) measurements, the upstream electron number density is set to 500 cm^{-3} (Kurth et al., 2001), as derived from the upper hybrid resonance emissions. The ion and electron temperatures read $k_B T_i = k_B T_e =$ 100 eV (Kivelson et al., 2004), resulting in an upstream plasma mass density and internal energy density of 6.166×10^9 amu m^{-3} and 16.02×10^{-9} J m^{-3}, respectively.

3.2 Plasma Sources and Losses

According to Saur et al. (1998), the dominant ionization process in Europa's atmosphere is electron impact ionization, which is more than one order of magnitude larger than photoionization. Therefore, in our model the neutral atmosphere and plume are only ionized by electron impacts, and two ionospheric singly charged ion populations with masses $m_{O_2^+} = 32$ amu and $m_{H_2O^+} = 18$ amu are produced. The ion production rates for O_2 and H_2O are calculated by multiplying the respective neutral density by a given ionization rate, in analogy to Blöcker et al. (2016), Jia et al. (2018), and Arnold et al. (2019). We adopt constant electron impact ionization rates of $f_{\text{imp}} = 2{\times}10^{-6}$ s^{-1} for both ${O_2}^+$ and H_2O^+ production, within the range derived by Smyth and Marconi (2006), and analogous to the values employed by Arnold et al. (2019) and Arnold et al. (2020).

Dissociative recombination between ions and electrons is the main loss process in our model. We account for the loss of ionospheric O_2^+ and H_2O^+ with the recombination rate coefficients α_{rec} (in m^3 s^{-1}) given by Schunk and Nagy (2009):

$$\alpha_{\text{rec},O_2^+}(T_e) = 2.4 \times 10^{-13} \left(\frac{300}{T_e} \right)^{0.7}, \tag{11}$$

$$\alpha_{\text{rec},H_2O^+}(T_e) = 1.03 \times 10^{-9}\ T_e^{-1.111}. \tag{12}$$

For the calculation of α_{rec}, we use an ionospheric electron temperature T_e of 0.5 eV. In analogy to the approach of Duling et al. (2014), Blöcker et al. (2016), and Blöcker et al. (2018), we avoid that the plasma number density $n = \rho / m_i$ decreases below the background ion density n_0 by adopting the expression for the loss rate:

$$L = \begin{cases} \alpha_{\text{rec}} n \,(n - n_0) & \text{for } n > n_0 \\ 0 & \text{for } n < n_0 \end{cases} \tag{13}$$

from Saur et al. (2003).

The exchange of momentum between the plasma and Europa's atmosphere is modelled through the ion-neutral collision frequency:

$$\nu_n = \sigma_n v_0 n_n, \tag{14}$$

similar to Duling et al. (2014). Equation (14) is a function of the ion-neutral collision cross section σ_n, typical plasma bulk velocity v_0, and the number density n_n of O_2 and

H_2O molecules in the atmosphere. We employ an O_2 cross section of 2×10^{-19} m^{-2} as in Saur et al. (1998) and an H_2O cross section of 8×10^{-19} m^{-2} following equations (A2) to (A7) from Kriegel et al. (2014). Two different mechanisms are included in the total momentum transfer cross sections: induced dipole ion-molecule interactions and charge exchange.

3.3 Electromagnetic Induction in a Subsurface Water Ocean

Due to the $\sim$10° tilt of Jupiter's magnetic moment with respect to its spin axis, the x and y components of the Jovian background magnetic field vary periodically at Europa's location. This results in an inducing field with the 11.1 h synodic rotation period of Jupiter. The time-varying inducing background magnetic field, in units of nT, is given analytically as a function of system III longitude by (Schilling et al., 2007):

$$B_{0,x}(\lambda_{\mathrm{III}}) = -84\ \sin(\lambda_{\mathrm{III}} - 200^\circ), \tag{15}$$

$$B_{0,y}(\lambda_{\mathrm{III}}) = -210\ \sin(\lambda_{\mathrm{III}} - 200^\circ). \tag{16}$$

In comparison to the strong variations of the other two field components, $B_{0,z}$ is about an order of magnitude smaller (Seufert et al., 2011). This time-varying inducing background field drives currents in Europa's conductive subsurface water ocean, and therefore generates a time-varying induced dipolar magnetic field (Khurana et al., 1998; Saur et al., 2010). Considering a spatially homogeneous inducing magnetic field and a radially symmetric ocean, the induced field is dependent on the thickness, the conductivity, and the depth of the ocean beneath the surface. In accordance with Schilling et al. (2007) and Blöcker et al. (2016), we assume a 100 km thick ocean in 25 km depth, with an electric conductivity of $\sigma = 0.5$ S m^{-1}. The time-variable induced field within the subsurface ocean is included in the inner boundary conditions at the surface of Europa as discussed in section 3.5.

3.4 Numerical Solution Process

In order to solve the differential equations (7) to (10), we utilize a modified version of the three-dimensional publicly available ZEUS-MP MHD code, based on Duling et al. (2014) and also employed by Blöcker et al. (2016) and Blöcker et al. (2018) to describe Europa's and Io's plasma interaction, respectively. This open source code is a multiphysics, massively parallel, message-passing code first developed by Stone and Norman (1992b) and Stone and Norman (1992a), which solves the single-fluid, ideal MHD equations in three dimensions. ZEUS-MP uses a finite-difference staggered-mesh approach and applies a second-order accurate, monotonic advection scheme. The solution is computed by the code time forward and the time step is controlled by the Courant-Friedrichs-Lewy criterion. In addition, ZEUS-MP combines the Constrained Transport algorithm with the Method of Characteristics (MOC-CT) for the treatment of Alfvén waves. ZEUS-MP algorithms are described in detail in Stone and Norman (1992a), Stone and Norman (1992b), and Hayes et al. (2006).

We employ a spherical grid with $160 \times 360 \times 360$ (r, θ, ϕ) cells. The angular resolution is equidistant in θ and ϕ with $\Delta\theta = 0.5^\circ$ and $\Delta\phi = 1^\circ$. The radial resolution is not equidistant and we increase the radial grid spacing by a factor of 1.026 from cell to cell, between the inner ($r = 1\ R_E$) and the outer boundary ($r = 20\ R_E$), which results in a resolution at the surface equal to 13 km.

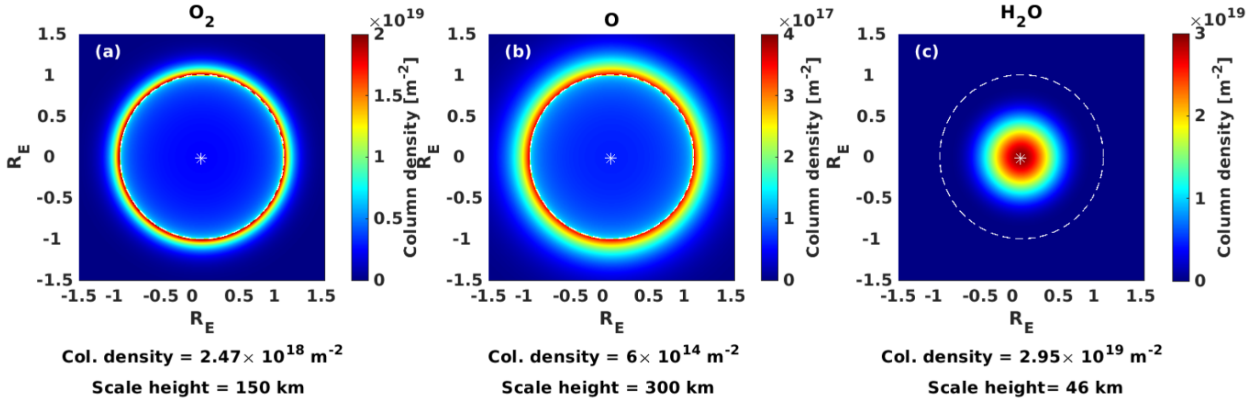

Figure 1. Line-of-sight integrated column density maps of the individual O_2, O, and stable H_2O distributions in the trailing hemisphere. The subsolar point is located at the center of the disk and is indicated with an asterisk. The vertical axis points towards North. The atmosphere parameters for each species are shown below each map. The column densities correspond to the values presented in Roth (2021). Note that the limits of the colorbar are different between panels.

3.5 Boundary Conditions

The two boundary areas of our simulation domain are the inner sphere at $r = 1\ R_E$ and the outer sphere at $r = 20\ R_E$. At the outer boundary we apply open boundary conditions for the four MHD variables ρ, $\mathbf{v}$, $\mathbf{B}$, and e. At the upstream region ($\phi \leq 180°$) the inflow method is used, while at the downstream region ($\phi > 180°$) the outflow method is applied. At the inner boundary, i.e., Europa's icy surface, plasma particles are assumed to be absorbed. Therefore we utilize open boundary conditions for $\mathbf{v}$, ρ, and e by an outflow method. The radial component of the plasma bulk velocity is set to $v_r \leq 0$ everywhere on the surface, as no plasma flows out of it. Furthermore, Europa's insulating icy surface also inhibits any electric currents penetrating it. Duling et al. (2014) derived boundary conditions for the magnetic field ensuring there is no radial electric current. In addition, the boundary condition also includes time-variable induction fields within electrically conducting subsurface layers.

4 Results

We now quantitatively investigate Europa's interaction with its plasma environment by means of the atmospheric and MHD models presented in the previous sections. First, we show our neutral gas distributions and their two-dimensional emission patterns, and then, we present the respective oxygen emission ratio profiles. Finally, we compare our MHD simulations with the Galileo magnetic field data along the trajectory of the E12 flyby.

4.1 Oxygen Emission Ratio Profile

We start by reproducing the observed radial profile of the oxygen emission ratio r_γ presented in Roth (2021), with an atmosphere model consisting of O_2, O, and stable H_2O, as described in Section 2.1. Figure 1 shows maps of column density in the trailing hemisphere for each species, after integrating the neutral gas distributions along the line of sight with the subsolar point in the center of the disk. A cosine to the tenth-power on the angle to the subsolar point (i.e., $\beta = 10$) is assumed for the H_2O model (panel (c)).

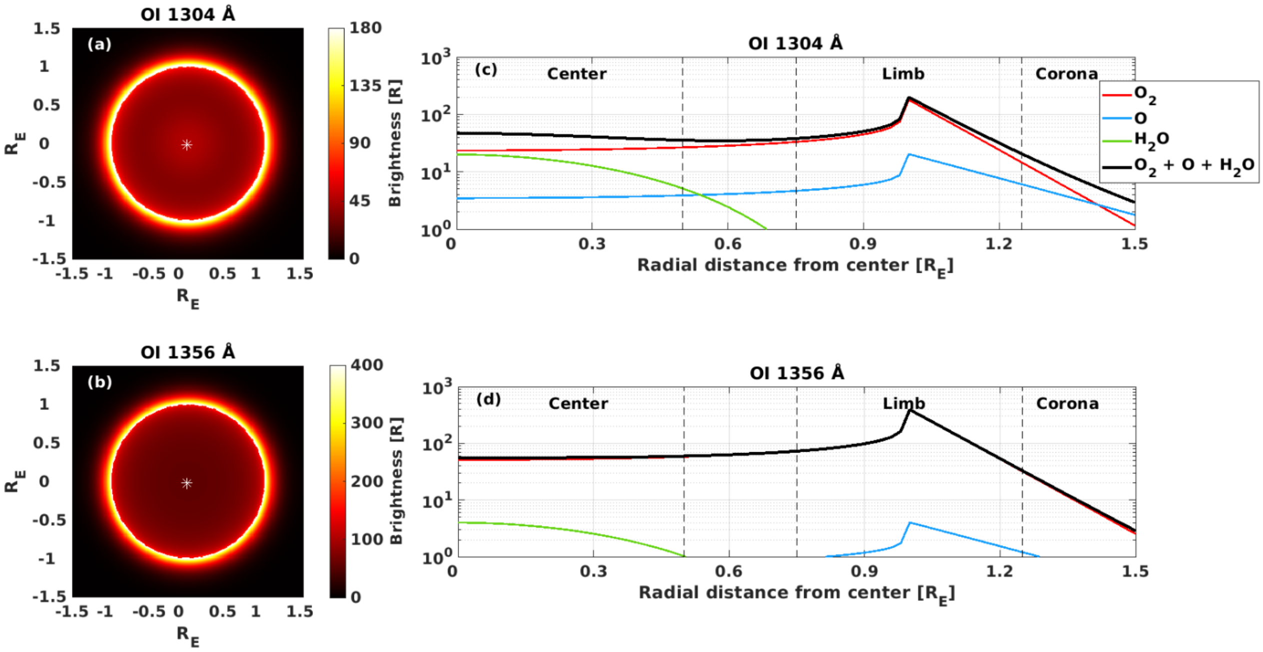

Figure 2. (a) and (b) Images of the oxygen emission at 1304 Å and 1356 Å above Europa's trailing hemisphere for the total O_2 + O + H_2O atmosphere model. The subsolar point is located at the center of the disk and is indicated with an asterisk. The vertical axis points towards North. (c) and (d) Radial profiles of the average 1304 Å and 1356 Å brightness within concentric rings from the disk center out to 1.5 R_E. The profiles are shown for the total atmosphere and for the individual contributions from O_2, O, and H_2O.

The two-dimensional emission patterns for the total $O_2 + O +$stable H_2O atmosphere model that result from the line-of-sight integration over the local intensities (Section 2.2) are presented in panels (a) and (b) of Figure 2, for both OI 1304 Å and OI 1356 Å lines. These 361 × 361 pixel images, with a spacing of 0.01 R_E, mainly reflect limb brightening from the global O_2 and O, with a minor contribution from H_2O to the total OI 1304 Å emission. The averaged simulated radial profiles in 0.025 R_E wide concentric rings (panels (c) and (d)) show contributions from the three neutral gases to the total OI 1304 Å brightness, with the emissions of H_2O being comparable to those of O_2 close to the center of the disk. In contrast, at 1356 Å, H_2O and O yield emissions which are more than one order of magnitude lower than those of O_2, and thus the total averaged OI 1356 Å profile across the disk vastly originates from the latter.

The observed and simulated oxygen emission ratio profiles r_γ are shown in Figure 3 (black and red lines, respectively). The maximum of both profiles is in the radial bins close to 1 R_E, where the contributions from O and H_2O to the OI 1304 Å emissions are the lowest. At radial distances above the limb ($>$ 1 R_E), the abundance of O results in a higher 1304 Å than 1356 Å intensity, therefore reducing the ratio r_γ. The oxygen emission ratio also decreases towards the disk center, due to the increase in the H_2O column density and hence, in the emission due to H_2O. It is worth emphasizing that Roth (2021) do not report any H_2O plumes active during the HST observations from which the oxygen emission ratio was derived, and therefore we do not take them into account in our simulated radial profile of r_γ. However, following the in-situ evidence provided by Jia et al. (2018) for the E12 flyby, we include a plume in the subsequent MHD modelling of the plasma interaction in the vicinity of the moon, as presented in Section 2.1.

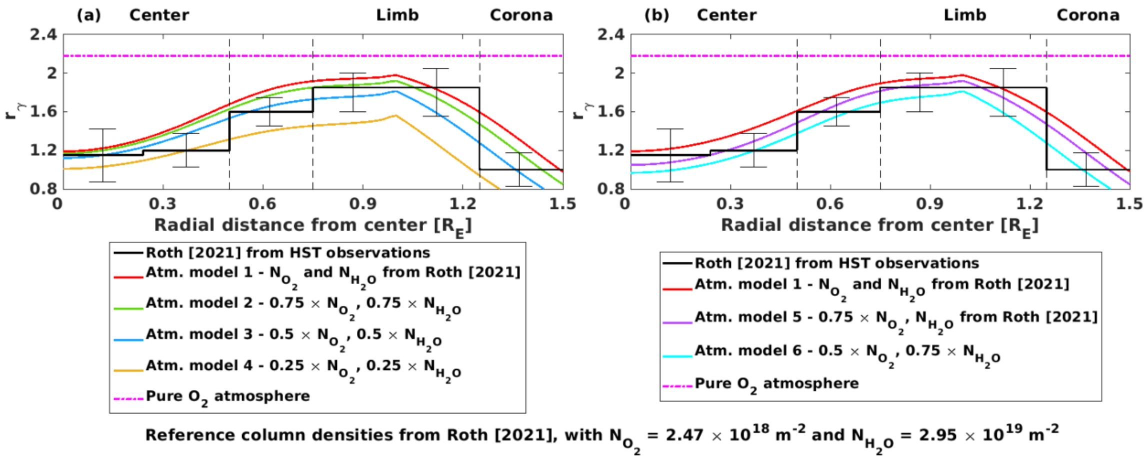

Figure 3. Radial profile of the oxygen emission ratio of OI 1356 Å to OI 1304 Å for HST observations (black histogram) and for our simulated O_2 + O + H_2O atmosphere models with varying O_2 and H_2O column densities, as percentages of the values calculated by Roth (2021). In panel (a) both column densities are decreased by the same rate, whereas in panel (b) the rate is different.

Table 1. O_2 and H_2O column densities for different atmosphere models, as percentages (indicated in parenthesis) of the original values in Roth (2021). The last column provides the abundance of H_2O relative to O_2.

Atmosphere model	N_{O_2} ($\times 10^{18}$ m^{-2})	N_{H_2O} ($\times 10^{19}$ m^{-2})	N_{H_2O}/N_{O_2}
1	2.47 (100%)	2.95 (100%)	11.94
2	1.85 (75%)	2.22 (75%)	11.94
3	1.24 (50%)	1.47 (50%)	11.94
4	0.62 (25%)	0.74 (25%)	11.94
5	1.85 (75%)	2.95 (100%)	15.95
6	1.24 (50%)	2.22 (75%)	17.9

The oxygen emission ratio derived from HST images by Roth (2021) is provided with uncertainties along its radial profile, and therefore we seek further models that lie within the error bars of the observations. In addition, Roth (2021) also restricted the abundance of H_2O relative to O_2 between 12 and 22. With these constraints in mind, we calculate the emission ratio for three additional atmosphere models, in which we successively reduce the column densities of O_2 and H_2O and multiply both original values in Roth (2021) by 0.75, 0.5, and 0.25, as Table 1 indicates (models 2 to 4). The column densities of both neutrals are decreased by the same percentage in each model, and therefore the abundance of H_2O with respect to O_2 is 11.94 in all cases, consistent with the range obtained by Roth (2021). The scale heights of both species do not vary within models, i.e., H_{O_2} and H_{H_2O} were kept constant. Rather, the surface number density is recalculated for each case, as the column density is given by the product of the assumed scale height and the surface number density. Panel (a) of Figure 3 shows that the profiles from models 2 to 4 also exhibit the same pattern across the disk mentioned before for model 1: maximum in the bins close to the limb, and decrease towards the center and above the limb. However, the r_γ profile for the model with the original column densities (1, in red) falls out of the error bars provided by Roth (2021) in the bins between

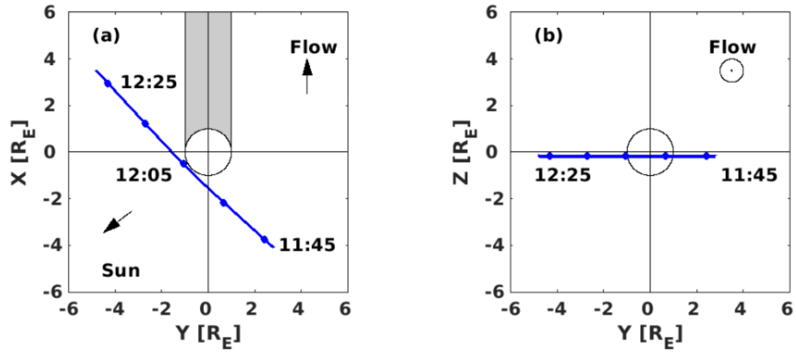

Figure 4. E12 flyby trajectory in the (a) XY and (b) YZ planes. The gray shaded region in panel (a) indicates Europa's downstream geometric wake.

the center and the limb, while the profile for the case with 25% of the column densities (4, in yellow) diverges significantly from the observations beyond ∼0.5 R_E.

Furthermore, we also examine models in which the column densities of O_2 and H_2O are decreased with respect to the original values in Roth (2021) by different percentages. We find two combinations of column densities that yield ratios N_{H_2O}/N_{O_2} within 12 to 22, and these are included as models 5 and 6 in Table 1. As can be seen in panel (b) of Figure 3, both fit the observed profile of r_γ within its uncertainties. Since in these two models the abundance of H_2O is decreased by a smaller percentage than O_2, the simulated emission ratio is displaced below the observed profile, reaching values close to 1 in the center of the disk, as this is the location in which we concentrate our H_2O atmosphere (i.e., the subsolar point).

With the results presented in this section, we identify several O_2 and H_2O column densities that fulfill the observed oxygen emission ratio r_γ within its error bars. The MHD simulations presented in the next section will provide additional information to constrain the abundance of these species in Europa's neutral atmosphere.

4.2 MHD Simulations of Galileo E12 Flyby

We now simulate Europa's interaction with its plasma environment for the conditions of the Galileo E12 flyby, as described in Section 3. Out of the eight targeted passes in which MAG data was acquired, this flyby came closest to the surface (196 km). In addition, this pass crossed the trailing sunlit hemisphere of Europa near the equator (−8.6°), where the abundance of the stable H_2O detected by Roth (2021) is expected to be maximum. The geometry of this flyby, illustrated in Figure 4, makes it ideal to test our candidate atmospheric models, and in particular, to elucidate the contribution of H_2O located around the subsolar point to the plasma interaction. The E12 pass occurred on 16 December 1997 and remained below 400 km altitude between 12:00:59 and 12:05:37 UT, with closest approach to Europa's surface at 12:03:20 UT (Kivelson et al., 1999; Jia et al., 2018). In addition, Galileo's trajectory was the closest to the subsolar point at 12:03:54 UT. The spacecraft traversed upstream in the plasma flow at the center of the plasma torus, with magnetic latitude relative to Jupiter's magnetic equator of −0.8°. Europa's system III longitude at the time of the flyby was 118°.

The magnetometer data for E12 flyby is shown in Figure 5. The magnetic field was unusually large upstream of Europa. From ∼12:00 UT to ∼12:03 UT, all three components of the magnetic field fluctuated. The sudden perturbations by hundreds of nT about

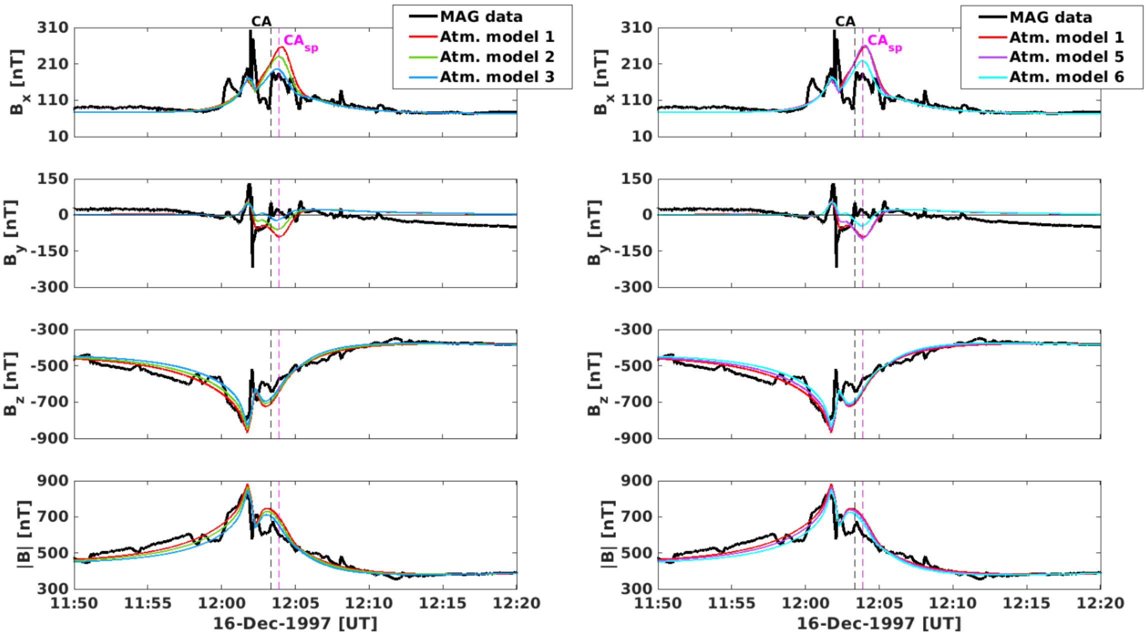

Figure 5. Galileo E12 flyby. Black lines show MAG data. Color coded are different simulations with varying O_2 and H_2O densities. In the left column, values are reduced by the same percentage of O_2 and H_2O, whereas in the right, the mixing rate of O_2 and H_2O has been changed. Properties of the atmospheric models are listed in Table 1. The vertical dashed black and magenta lines indicate Galileo's closest approach to Europa's surface (CA) and Galileo's closest approach to the subsolar point (CA_{sp}), respectively.

one minute before closest approach were attributed by Jia et al. (2018) to the passage of Galileo through a water plume.

In this study we aim to answer if the perturbation after closest approach, between ∼12:03:30 UT and ∼12:05:30 UT, mainly evident as a local maximum in the B_x component, is imposed by the presence of a stable H_2O atmosphere located at the subsolar point. In order to test this hypothesis we conduct several MHD simulations, in which we assume a neutral atmosphere consisting of global O_2, H_2O localized at the subsolar point (with $\beta = 10$), and a plume (as described in Section 2.1). The column densities of the first two components are varied according to the atmospheric models 1 to 6 presented in the previous section, whereas the properties of the plume are kept constant in all simulations.

Figure 5 compares the magnetic field measured by Galileo with the model results extracted from the simulations along the spacecraft trajectory. The left column shows the cases in which the densities of O_2 and H_2O at the subsolar point are kept as in Roth (2021) or both are decreased keeping the mixing ratio constant (atmospheric models 1, 2, and 3). The results of the scenario with densities reduced to 25% are not shown, since model 4 provided a poor fit to the observed oxygen emission ratio. The panels on the right hand side of Figure 5 present the results for the models in which the mixing rates are not constant (models 5 and 6).

In the dense H_2O atmosphere confined around the subsolar point, electron impact ionization and ion-neutral collisions are enhanced, and therefore, stronger magnetic field perturbations are generated. In all our simulations, perturbations are observed after clos-

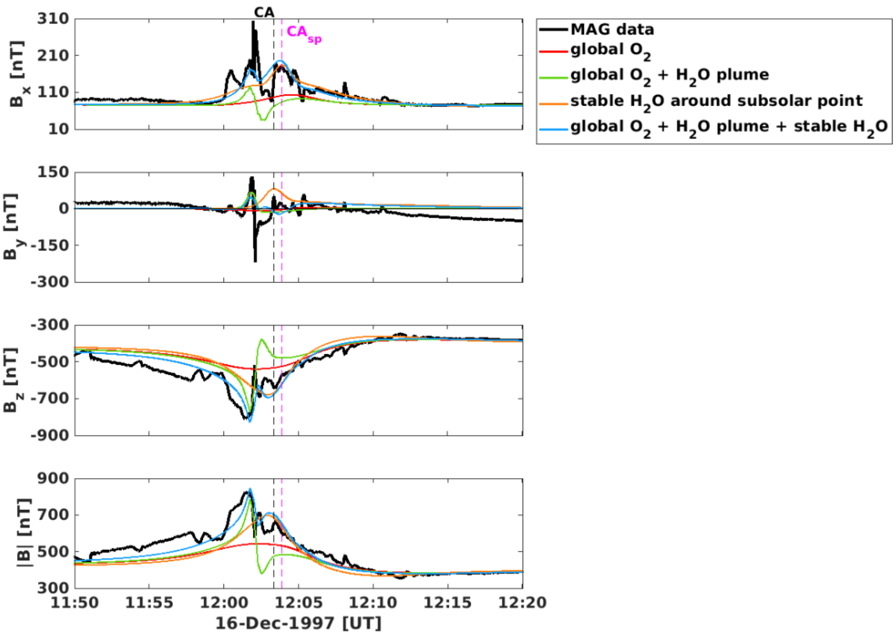

Figure 6. Contributions of O_2 and H_2O atmospheric components. The black line indicates Galileo MAG data; and the red, green, orange, and blue lines give the simulated magnetic fields for the E12 flyby trajectory assuming different atmospheric constituents. The column densities of O_2 and H_2O at the subsolar point correspond to atmospheric model 3.

est approach, in accordance with MAG data. In particular, the largest perturbation in the x component takes place around Galileo's closest approach to the subsolar point, where Roth (2021) suggested the stable H_2O distribution to be maximum. However, the predicted B_x fluctuations are largely overestimated ($>$ 40 nT) by atmospheric models 1, 2, and 5, namely those with both O_2 and H_2O column densities $\geq$ 75% from the values derived by Roth (2021). Model 3, with densities reduced by 50% provides the best fit to the perturbations after closest approach, deviating 13 nT at the location of the local maximum in B_x. Model 6 predicts variations with amplitudes between those of models 2 and 3. Similarly to B_x, the B_y component is best reproduced with model 3, whereas the remainder of the models do not provide a satisfactory fit to the measurements. B_z produces similar magnetic field responses in all cases. Therefore, we deem B_x as the most diagnostic component to identify model 3 as the best out of the six candidates. As the parameters of the plume (column density, location, and tilt) do not vary between simulations, the abrupt large-amplitude fluctuations linked to this feature are similar in all cases.

In Europa's atmosphere, molecular O_2 is distributed approximately uniformly around the moon, whereas H_2O is present as a confined component, either in the form of sporadic plumes or a stable concentration around the subsolar point. In order to better understand the effects of the individual contributions of each species on the plasma interaction, we perform further MHD simulations with atmospheric model 3 by successively adding, one at a time, each element of our three-component atmosphere (Figure 6). We start by considering only a global radially symmetric O_2 distribution. Since our O_2 column density is in the lower end of the typical range between 2 and 15×10^{18} m^{-2} (Hall et al., 1995, 1998; McGrath et al., 2009; Roth et al., 2014) there is very little contribution from this species to the plasma interaction. The variations around closest approach are of low amplitude, ∼30 nT and ∼100 nT in x and z respectively, relative to the background values. The addition of the water plume to our model predicts the abrupt and rapid fluctuation of magnetic field prior to closest approach, similar to the simulations in Jia et al. (2018). However, the variations between ∼12:03 UT and ∼12:06 UT are not reproduced by the model, as can be seen in e.g. B_x and the total field $|B|$.

The individual contribution of the stable H_2O atmosphere centered at the subsolar point is mainly evident as a local maximum in B_x, where the magnetic field is enhanced by 80 nT just after closest approach. The perturbation in the modelled x component is concurrent with the observed fluctuations, and both lie within the region where the H_2O distribution is predicted to be the most abundant, i.e., the subsolar point. Our H_2O atmosphere also reproduces some of the variations observed in B_y and the gradual recovery of B_z after closest approach.

Lastly, when all three atmospheric constituents are taken into account, two substructures of a confined nature are evident in B_x. Such features cannot be produced by a globally distributed O_2, and are therefore indicative of a localized component, as is the case of water. Between the occurrence of the plume and the stable H_2O, just before closest approach, the measured B_x and B_y components decrease abruptly, while B_z is enhanced. However, our simulations do not reproduce such variations as markedly as the MAG data show. We interpret this lack of agreement as a consequence of our parametrization of the water plume, which does not fully resolve the perturbed magnetic field nor the sharpness of the gradients adjacent to this structure. Nevertheless, the focus of our study is after the time of closest approach, when the signature of H_2O centered around the subsolar point is present in the data and our simulations.

5 Discussion

Our MHD simulations demonstrate that both O_2 and H_2O column densities have to be reduced by 50% with respect to the values in Roth (2021) and lie within the error bars of the observed oxygen emission ratio, in order to fulfill the conditions posed by HST and MAG data. In this section we assess the robustness of this finding by varying certain parameters of the atmospheric and MHD models (H_2O distribution and electron impact ionization, respectively) and performing three sets of additional simulations.

At first, we vary the degree of confinement of H_2O around the subsolar point, as described by the exponent β of the cosine term in equation (2). The results presented previously employed $\beta = 10$, and we examine four additional cases: $\beta = 2, 4, 6$, and 8. Figure 7 shows the H_2O column density as a function of longitude from the subsolar point for the five values of β. All the distributions peak at the subsolar point, at 12 Local Time (LT), but decrease at a different rate away from it. For example, in the least confined H_2O atmosphere ($\beta = 2$), the column density reaches half of its maximum value ($N_{H_2O} = 0.75 \times 10^{19}$ m^{-2}) at 45° away from the subsolar point, whereas in the most localized case ($\beta = 10$), such an H_2O column density is observed 22° away from it. In addition, the rate of decrease of the stable H_2O abundance differs less markedly between the cases with the largest exponents.

The line-of-sight integrated column density of the stable H_2O component with the three most confined distributions ($\beta = 6, 8$, and 10) is illustrated in Figure 8. For ease of comparison among the three cases, contours corresponding to column densities of 1.4, 0.75, and 0.375×10^{19} m^{-2} are overlaid. These values indicate 95%, 50%, and 25% of the maximum abundance at the subsolar point, respectively. As expected, the radial extent of the H_2O distribution is more confined with increasing β. For the exponent $\beta =$ 6, the contour with column density of 1.4×10^{19} m^{-2} is located at 0.18 R_E from the center, whereas for $\beta = 10$, this contour is found at 0.1 R_E. For the column density

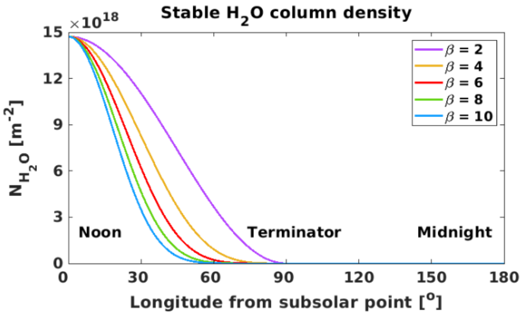

Figure 7. Degree of confinement of the H_2O component. Column density distribution as a function of longitude from the subsolar point for different values of the exponent β.

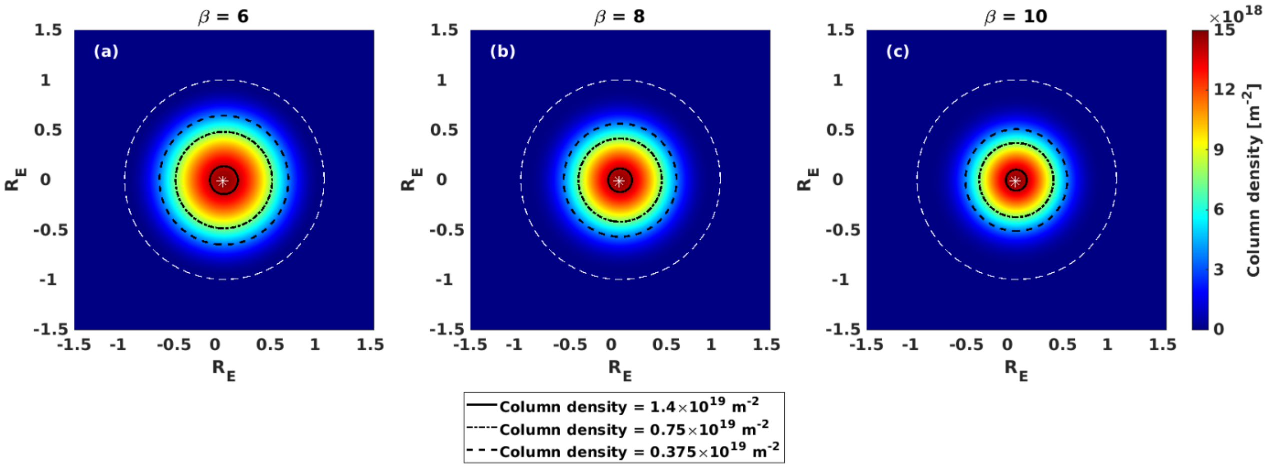

Figure 8. Degree of confinement of the H_2O component. Line-of-sight integrated column density maps in the trailing hemisphere for the indicated values of the exponent β. The subsolar point is located at the center of the disk and is indicated with an asterisk. The vertical axis points towards North. Black contours indicate column densities of 95% (solid), 50% (dashed-dotted), and 25% (dotted) of the maximum at the disk center, corresponding to 1.4, 0.75, and 0.375×10^{19} m^{-2}, respectively.

equal to $0.375{\times}10^{19}$ m^{-2}, the contours extend from 0.51 R_E ($\beta = 10$) to 0.67 R_E ($\beta = 6$).

In analogy to Section 4.1, we start by calculating the oxygen emission ratio for the total O_2+O+stable H_2O atmosphere model. Panel (a) of Figure 9 shows the profiles for the five cases of β. The least confined distribution, with $\beta = 2$, does not match the observed r_γ profile beyond ∼0.5 R_E. The remainder of the exponents provide a satisfactory fit to the HST observations within the error bars across the entire disk, and they yield similar values of r_γ at the central bins. Nonetheless, the profiles diverge the most between 0.3 and 0.8 R_E, where the H_2O in the model with $\beta = 4$ is the least confined, and thus r_γ is the lowest.

After assessing to what extent these distributions are consistent with the HST observations, we use them to conduct MHD simulations of the plasma interaction (Figure 10, left column). It must be emphasized that the only parameter that differs among them

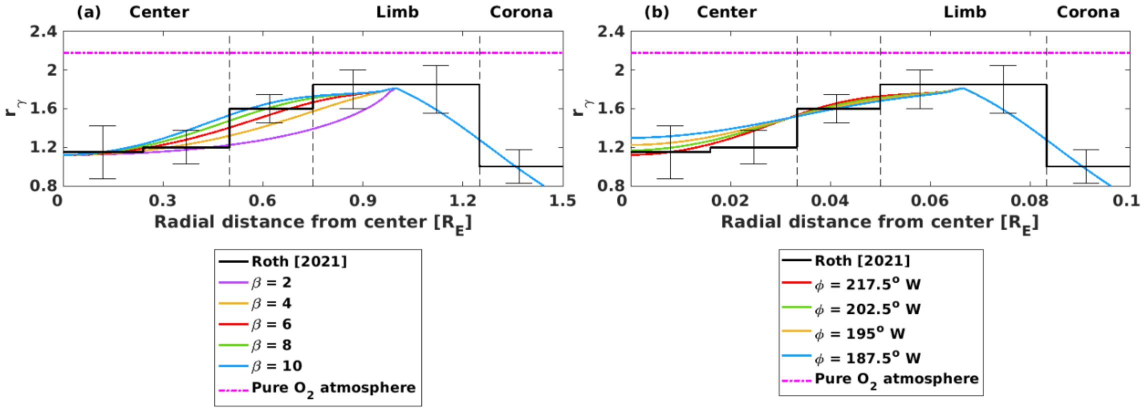

Figure 9. Sensitivity analysis of the stable H_2O atmosphere: degree of confinement and location of maximum. Radial profiles of the observed and simulated oxygen emission ratio for our O_2 + O + H_2O atmosphere model with O_2 and H_2O column densities 50% from the values in Roth (2021). Panel (a) presents the results for different values of the exponent β in the H_2O distribution, and panel (b) for various locations of the center of the H_2O component (longitude ϕ).

is the exponent β. In all cases, the simulated magnetic field at the time of closest approach to the subsolar point is comparable in amplitude, as this is the location at which the stable H_2O column density reaches its maximum for the five β values. The field magnitude for $\beta = 2$ is only marginally larger by $\sim$20 nT with respect to the model with $\beta = 10$, since an H_2O atmosphere with lower β is spatially wider, contains more neutrals available for collisions, and therefore generates larger magnetic field perturbations. We have also explored other functional forms describing narrower H_2O distributions, e.g., exponential or trigonometric multiplied by a scalar, but the resulting oxygen emission ratio diverges from the observed profile at the center of the disk and does not fit it within its uncertainties. All in all, the similarity among our five simulations in the left panel of Figure 10 shows that the exact value of β and the spatial extent of the stable H_2O cannot be uniquely constrained with the MAG data, thereby highlighting the importance of simultaneously exploring the structure and density of the atmosphere with the HST spectral images.

A second parameter that we vary is the location of the center of the stable H_2O component. Our previous simulations assume that the maximum H_2O abundance is aligned with the instantaneous subsolar point. However, thermal inertia of Europa's icy surface might shift the location with the largest temperature, and thus of the maximum H_2O density, with respect to the subsolar point. To investigate this, we displace the center of the H_2O distribution in longitude from $\phi = 217.5°$ W (corresponding to 12 LT), towards the east (in the afternoon sector), by 15°, 22.5°, and 30°. As in the previous case, we first make certain that these models are consistent with the HST data by calculating the oxygen emission ratio (panel (b) of Figure 9). The four profiles fit the observed r_γ within its uncertainties in all the bins except between 0.25 and 0.5 R_E, where the modelled values for the cases with $\phi = 195°$ W and $\phi = 187.5°$ W (corresponding to 1.5 and 2 hours after 12 LT) fall out of the error bars by 0.75 of r_γ. In the central bin, between 0 and 0.25 R_E, and for the atmosphere with H_2O coincident with the subsolar point at 12 LT (in red), r_γ is the lowest. For the model with the most displaced H_2O distribution (in blue), the H_2O density at the center of the disk is lower, O_2 dominates, and thus r_γ is larger by 0.17. The opposite pattern is observed at the limb, between 0.6 and

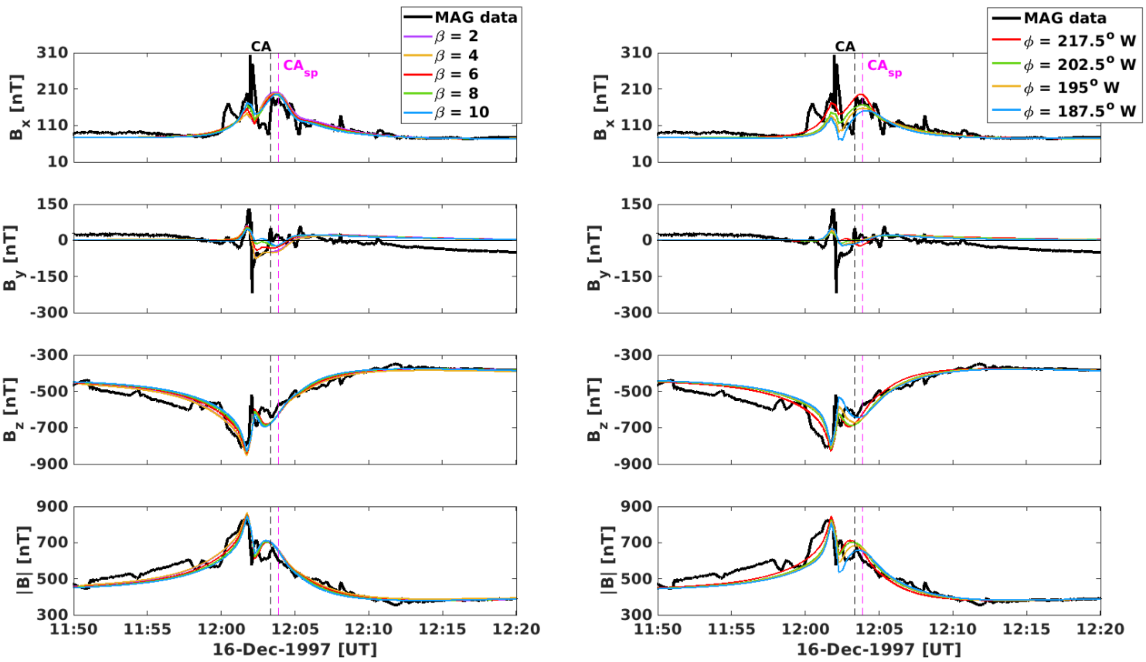

Figure 10. Sensitivity analysis of the stable H_2O atmosphere: degree of confinement and location of maximum. The black line indicates Galileo MAG data for the E12 flyby trajectory. Color coded are different simulated magnetic fields for various values of β in the H_2O distribution (left column) and locations of the center of the H_2O component (longitude ϕ, right column).

0.9 R_E, where the profile for the non-displaced subsolar point is larger by 0.07 relative to the most displaced one. The location at which this trend reverses is ~0.48 R_E.

The panels on the right hand side of Figure 10 compare the magnetic field measured by MAG and the predicted field with different locations of the maximum of the stable H_2O compared to the subsolar point. The remainder of the parameters stay unchanged between simulations. The four cases reproduce the local maximum in B_x after closest approach, consistent with the presence of H_2O at this location. As already mentioned, our initial simulation with the H_2O abundance centered at the subsolar point overestimates the observed field by ~13 nT in the x component. On the contrary, the other three simulations, with the displaced stable H_2O distribution, underestimate the measured B_x by ~16 nT ($\phi = 202.5°$ W) and ~32 nT ($\phi = 187.5°$ W). The occurrence of the local maximum is also displaced from 12:03:46 UT for $\phi = 217.5°$ W to 12:04:10 UT for $\phi = 187.5°$ W. The other two components are also reproduced similarly with the different H_2O models. The field magnitude $|B|$ decreases abruptly after the peak due to the plume (at 12:01:40 UT) by 207 nT and 271 nT in the simulations with the maximum H_2O at 12 LT and 2 hours after, respectively. Both values are in accordance with the observed decrease of 248 nT. In analogy to B_x, the local maximum in $|B|$ around closest approach occurs the earliest in the simulation with the stable H_2O centered at the subsolar point. Our findings show that the plasma interaction is sensitive to the location of the H_2O atmosphere, whose center might be misaligned with respect to the subsolar point.

The simulations with $\phi = 217.5°$ W and $\phi = 202.5°$ W are the best constrained both by HST and MAG measurements. For the latter case, the location of the H_2O maximum is displaced one hour after 12 LT. Therefore, our results suggest that the plasma interaction for the H_2O atmosphere is partly dictated by Europa's surface temperature, which in turn controls the sputtering and sublimation yield of water ice (Famá et al., 2008; Plainaki et al., 2013; Vorburger & Wurz, 2018). These findings also hint that thermal inertia might play a role in the location of the H_2O atmosphere.

The stable H_2O distribution is concentrated in the vicinity of the subsolar point, but its column density is too large as expected from standard temperature maps of Europa's surface. An H_2O column density of $N_{H_2O} = 1.47 \times 10^{19}$ m^{-2} would require a temperature of 142 K, in contrast to the observed maximum dayside value of 132 K (Spencer et al., 1999). The modelling works of Smyth and Marconi (2006) and Vorburger and Wurz (2018) have considered both sublimation and sputtering as sources. Assuming surface temperatures between 95 and 132 K, their predicted H_2O column densities lie between 2 and $6{\times}10^{16}$ m^{-2}. Therefore, an additional mechanism is required to explain this density surplus. Roth (2021) speculated that sputtering and secondary sublimation might be the origin of the detected stable H_2O atmosphere, in line with the results of Teolis et al. (2017).

As pointed out by Roth (2021), the derived abundances of O_2, O, and H_2O in their model are sensitive to the assumed electron properties, i.e., density and temperature. The electron impact ionization rate f_{imp} depends on the density of neutrals and electrons, but also non-linearly on the temperature of the impinging electrons (Blöcker et al., 2016). We therefore investigate the sensitivity of our results to the assumed value of f_{imp}. We conduct two simulations in which the ionization rate of both ${O_2}^+$ and H_2O^+ is multiplied by 0.5 in the first one ($f_{\text{imp}} = 10^{-6}$ s^{-1}), and by 2 in the second one ($f_{\text{imp}} = 4\times 10^{-6}$ s^{-1}). Both values are within (or close to) the range provided by Smyth and Marconi (2006). As before, the assumed atmospheric model is number 3 from Section 4.1, namely O_2 and H_2O column densities 50% of the values derived from Roth (2021), and an H_2O distribution with $\beta = 10$ and centered at the subsolar point.

Figure 11 presents the simulated magnetic field for these three scenarios. All the components of the magnetic field are perturbed at the location of the H_2O atmosphere, albeit at different amplitudes. The case with ionization rate $f_{\text{imp}} = 4{\times}10^{-6}$ s^{-1} overestimates the local maximum due to the H_2O atmosphere in the x component by ∼31 nT, whereas with $f_{\text{imp}} = 10^{-6}$ s^{-1} the predicted B_x only differs by ∼5 nT from the observations. The perturbations in B_y, both due to the plume and the H_2O around the subsolar point, are of larger amplitude for the case with $f_{\text{imp}} = 4 \times 10^{-6}$ s^{-1}, diverging the most from the observed field, especially after the plume occurrence. A similar pattern is evident in the B_z component, where the model with $f_{\text{imp}} = 4 \times 10^{-6}$ s^{-1} overestimates the minimum due to the plume by ∼65 nT, whereas the other two cases only differ from the observed value by ∼16 nT. The local minimum in B_z around closest approach is reproduced well by the three ionization rates.

Our parameter study demonstrates that O_2 and H_2O column densities reduced by 50% relative to Roth (2021) consistently match the amplitude and the location of the observed magnetic field perturbations. In other words, our simulations invariably require low column densities, but still within the error bars of the r_γ profile of Roth (2021), to be in agreement with the MAG data. Most importantly, this conclusion holds after considering uncertainties in our atmospheric and MHD model, such as the location of the H_2O distribution and the electron impact ionization rate.

Our results also show that variations of O_2 and H_2O densities by a factor of 2 (Figure 5) result in larger magnetic field perturbations than those due to an increase in the ionization rate by the same factor (Figure 11). This pattern suggests that, for our specific simulation of Galileo E12 flyby, the effect of electron impact ionization is weak, and thus, ion-neutral collisions play a dominant role in the overall plasma interaction.

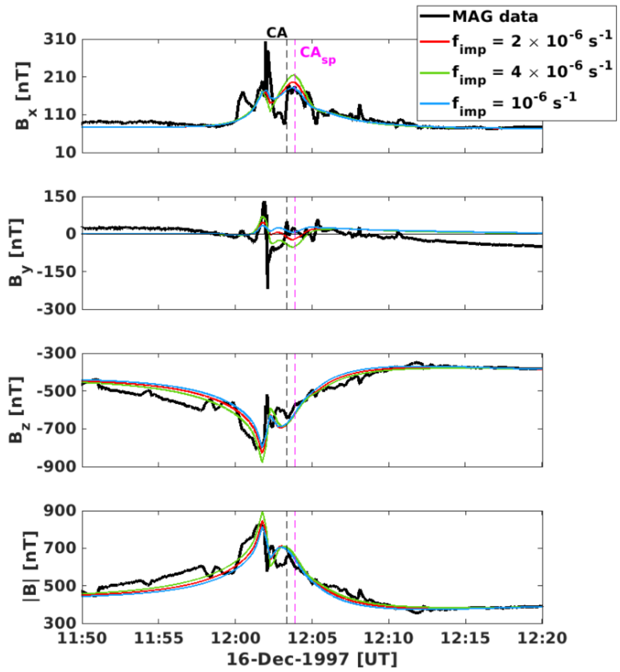

Figure 11. Sensitivity analysis of the electron population. The black line indicates Galileo MAG data for the E12 flyby trajectory. Color coded are different simulated magnetic fields for various values the electron impact ionization rate f_{imp}.

6 Summary and Conclusions

In this work, we present new constraints on the density and spatial distribution of O_2 and H_2O at Europa's atmosphere using a joint set of observations: HST spectral images of the trailing side of the moon, and Galileo magnetometer data for E12 flyby. We study the effect of a stable H_2O component concentrated around the subsolar point on the moon's plasma interaction. In addition, we perform a parameter study of the H_2O distribution and the electron impact ionization rate.

We describe Europa's atmosphere with three neutral species: O_2, O, and H_2O; and we obtain several distributions by progressively reducing the original O_2 and H_2O column densities from Roth (2021). We find that several of the assumed abundances fit the observed oxygen emission ratio profile from HST within its error bars. In addition, we use a single-fluid MHD model to simulate the plasma interaction with Europa's atmosphere. Our results show that only O_2 and H_2O column densities 50% from the values in Roth (2021), i.e., 1.24×10^{18} m^{-2} and 1.47×10^{19} m^{-2} respectively, jointly fulfill both HST and MAG data. By doing so, we use Galileo magnetic field measurements to provide additional constraints on Europa's atmosphere, and we limit the neutral gas densities to their lower end.

We show that the magnetic field fluctuations observed by Galileo after closest approach, mainly evident as a local maximum in B_x, are a signature of a confined H_2O atmosphere around the subsolar point. Furthermore, the parameter study demonstrates that our decreased densities perform well with a variety of H_2O and electron properties. As a consequence, a good agreement between MAG observations and the MHD simulations always requires low O_2 and H_2O column densities, within the error bars of Roth (2021).

Our findings are significant in a number of ways. We provide the first evidence of a localized persistent H_2O atmosphere concentrated around the subsolar point in Galileo magnetometer data, and we jointly limit its density by employing two independent datasets. Our derived constraints on the location and abundance of the H_2O distribution will help to understand the origin of such stable component. Finally, both JUICE (Grasset et al., 2013) and Europa Clipper missions (Howell & Pappalardo, 2020) will conduct several low-altitude passes above Europa's surface. Our results provide the mission teams with valuable information on the location and density of a stable H_2O atmosphere on the moon's trailing hemisphere. In-situ plasma and magnetic field measurements, particularly those in the subsolar region, will place additional observational constraints and refine our characterization of Europa's neutral atmosphere.

7 Open Research

The ZEUS-MP code is publicly available and can be downloaded from `http://www.netpurgatory.com/zeusmp.html`. The Galileo Magnetometer data were retrieved from the NASA Planetary Data System at GO-J-MAG-3-RDR-HIGHRES-V1.0 (doi: 10.17189/1519667). The location of the subsolar point was determined using the `solar_system_v0039.tm` meta-kernel provided by JPL.

Acknowledgments

This project that has received funding from the European Research Council (ERC) under the European Union's Horizon 2020 research and innovation programme (grant agreement no. 884711). The numerical calculations have been performed on the CHEOPS Cluster of the University of Cologne, Germany. We thank Clarissa Willmes and Stefan Duling for their helpful advice on the usage of ZEUS-MP.

References

Arnold, H., Liuzzo, L., & Simon, S. (2019). Magnetic signatures of a plume at Europa during the Galileo E26 flyby. *Geophysical Research Letters*, *46*(3), 1149–1157.

Arnold, H., Liuzzo, L., & Simon, S. (2020). Plasma interaction signatures of plumes at Europa. *Journal of Geophysical Research: Space Physics*, *125*(1), e2019JA027346.

Bagenal, F., & Dols, V. (2020). The space environment of Io and Europa. *Journal of Geophysical Research: Space Physics*, *125*(5), e2019JA027485.

Bagenal, F., Sidrow, E., Wilson, R. J., Cassidy, T. A., Dols, V., Crary, F. J., ... Paterson, W. R. (2015). Plasma conditions at Europa's orbit. *Icarus*, *261*, 1–13.

Blöcker, A., Saur, J., & Roth, L. (2016). Europa's plasma interaction with an inhomogeneous atmosphere: Development of Alfvén winglets within the Alfvén wings. *Journal of Geophysical Research: Space Physics*, *121*(10), 9794–9828.

Blöcker, A., Saur, J., Roth, L., & Strobel, D. F. (2018). MHD modeling of the plasma interaction with Io's asymmetric atmosphere. *Journal of Geophysical Research: Space Physics*, *123*(11), 9286–9311.

Carr, M., Belton, M. J., Chapman, C. R., Davies, M. E., Geissler, P., Greenberg, R., ... others (1998). Evidence for a subsurface ocean on Europa. *Nature*, *391*(6665), 363–365.

Doering, J., & Gulcicek, E. (1989). Absolute differential and integral electron excitation cross sections for atomic oxygen 7. The 3 P→ 1 D and 3 P→ 1 S transitions from 4.0 to 30 eV. *Journal of Geophysical Research: Space Physics*, *94*(A2), 1541–1546.

Duling, S., Saur, J., & Wicht, J. (2014). Consistent boundary conditions at nonconducting surfaces of planetary bodies: Applications in a new Ganymede MHD model. *Journal of Geophysical Research: Space Physics*, *119*(6), 4412–4440.

Famá, M., Shi, J., & Baragiola, R. (2008). Sputtering of ice by low-energy ions. *Surface Science*, *602*(1), 156–161.

Grasset, O., Dougherty, M., Coustenis, A., Bunce, E., Erd, C., Titov, D., ... others (2013). JUpiter ICy moons Explorer (JUICE): An ESA mission to orbit Ganymede and to characterise the Jupiter system. *Planetary and Space Science*, *78*, 1–21.

Hall, D., Feldman, P., McGrath, M. A., & Strobel, D. (1998). The far-ultraviolet oxygen airglow of Europa and Ganymede. *The Astrophysical Journal*, *499*(1), 475.

Hall, D., Strobel, D., Feldman, P., McGrath, M., & Weaver, H. (1995). Detection of an oxygen atmosphere on Jupiter's moon Europa. *Nature*, *373*(6516), 677–679.

Harris, C., Jia, X., Slavin, J. A., Toth, G., Huang, Z., & Rubin, M. (2021). Multi-Fluid MHD Simulations of Europa's Plasma Interaction Under Different Magnetospheric Conditions. *Journal of Geophysical Research: Space Physics*, *126*(5), e2020JA028888.

Hartkorn, O., Saur, J., & Strobel, D. F. (2017). Structure and density of Callisto's atmosphere from a fluid-kinetic model of its ionosphere: Comparison with Hubble Space Telescope and Galileo observations. *Icarus*, *282*, 237–259.

Hayes, J., Norman, M. L., Fiedler, R. A., Bordner, J. O., Li, P. S., Clark, S. E., ... others (2006). Simulating radiating and magnetized flows in multiple dimensions with ZEUS-MP. *The Astrophysical Journal Supplement Series*, *165*(1), 188.

Howell, S., & Pappalardo, R. (2020). NASA's Europa Clipper—a mission to a potentially habitable ocean world. *Nature Communications*, *11*(1), 1–4.

Jia, X., Kivelson, M. G., Khurana, K. K., & Kurth, W. S. (2018). Evidence of a plume on Europa from Galileo magnetic and plasma wave signatures. *Nature Astronomy*, *2*(6), 459–464.

Johnson, R., Burger, M., Cassidy, T., Leblanc, F., Marconi, M., & Smyth, W. (2009). Composition and detection of Europa's sputter-induced atmosphere. *Europa, University of Arizona Press, Tucson*, 507–527.

Kabin, K., Combi, M., Gombosi, T., Nagy, A., DeZeeuw, D., & Powell, K. (1999). On Europa's magnetospheric interaction: A MHD simulation of the E4 flyby. *Journal of Geophysical Research: Space Physics*, *104*(A9), 19983–19992.

Kanik, I., Johnson, P., Das, M., Khakoo, M., & Tayal, S. (2001). Electron-impact studies of atomic oxygen: I. Differential and integral cross sections; experiment and theory. *Journal of Physics B: Atomic, Molecular and Optical Physics*, *34*(13), 2647.

Kanik, I., Noren, C., Makarov, O., Vattipalle, P., Ajello, J., & Shemansky, D. (2003). Electron impact dissociative excitation of O2: 2. Absolute emission cross sections of the OI (130.4 nm) and OI (135.6 nm) lines. *Journal of Geophysical Research: Planets*, *108*(E11).

Khurana, K., Kivelson, M., Stevenson, D., Schubert, G., Russell, C., Walker, R., & Polanskey, C. (1998). Induced magnetic fields as evidence for subsurface oceans in Europa and Callisto. *Nature*, *395*(6704), 777–780.

Kivelson, M., Bagenal, F., Kurth, W. S., Neubauer, F. M., Paranicas, C., & Saur, J. (2004). Magnetospheric interactions with satellites. *Jupiter: The planet, satellites and magnetosphere*, 513–536.

Kivelson, M., Khurana, K., Stevenson, D., Bennett, L., Joy, S., Russell, C., ... Polanskey, C. (1999). Europa and Callisto: Induced or intrinsic fields in a periodically varying plasma environment. *Journal of Geophysical Research: Space Physics*, *104*(A3), 4609–4625.

Kivelson, M., Khurana, K. K., Russell, C. T., Volwerk, M., Walker, R. J., & Zimmer, C. (2000). Galileo magnetometer measurements: A stronger case for a subsurface ocean at Europa. *Science*, *289*(5483), 1340–1343.

Kriegel, H., Simon, S., Meier, P., Motschmann, U., Saur, J., Wennmacher, A., . . . Dougherty, M. K. (2014). Ion densities and magnetic signatures of dust pickup at Enceladus. *Journal of Geophysical Research: Space Physics*, *119*(4), 2740–2774.

Kurth, W., Gurnett, D., Persoon, A., Roux, A., Bolton, S., & Alexander, C. (2001). The plasma wave environment of Europa. *Planetary and Space Science*, *49*(3-4), 345–363.

Makarov, O., Ajello, J. M., Vattipalle, P., Kanik, I., Festou, M., & Bhardwaj, A. (2004). Kinetic energy distributions and line profile measurements of dissociation products of water upon electron impact. *Journal of Geophysical Research: Space Physics*, *109*(A9).

McGrath, M., Hansen, C., & Hendrix, A. (2009). Observations of Europa's tenuous atmosphere. *Chapter in Europa. University of Arizona Press, Tucson*, *85*.

Plainaki, C., Cassidy, T. A., Shematovich, V. I., Milillo, A., Wurz, P., Vorburger, A., . . . others (2018). Towards a global unified model of Europa's tenuous atmosphere. *Space Science Reviews*, *214*(1), 1–71.

Plainaki, C., Milillo, A., Mura, A., Orsini, S., & Cassidy, T. (2010). Neutral particle release from Europa's surface. *Icarus*, *210*(1), 385–395.

Plainaki, C., Milillo, A., Mura, A., Orsini, S., Massetti, S., & Cassidy, T. (2012). The role of sputtering and radiolysis in the generation of europa exosphere. *Icarus*, *218*(2), 956–966.

Plainaki, C., Milillo, A., Mura, A., Saur, J., Orsini, S., & Massetti, S. (2013). Exospheric O2 densities at Europa during different orbital phases. *Planetary and Space Science*, *88*, 42–52.

Roth, L. (2021). A Stable H2O Atmosphere on Europa's Trailing Hemisphere From HST Images. *Geophysical Research Letters*, *48*(20), e2021GL094289.

Roth, L., Saur, J., Retherford, K. D., Strobel, D. F., Feldman, P. D., McGrath, M. A., & Nimmo, F. (2014). Transient water vapor at Europa's south pole. *Science*, *343*(6167), 171–174.

Roth, L., Saur, J., Retherford, K. D., Strobel, D. F., Feldman, P. D., McGrath, M. A., . . . Ivchenko, N. (2016). Europa's far ultraviolet oxygen aurora from a comprehensive set of HST observations. *Journal of Geophysical Research: Space Physics*, *121*(3), 2143–2170.

Rubin, M., Jia, X., Altwegg, K., Combi, M., Daldorff, L., Gombosi, T., . . . others (2015). Self-consistent multifluid MHD simulations of Europa's exospheric interaction with Jupiter's magnetosphere. *Journal of Geophysical Research: Space Physics*, *120*(5), 3503–3524.

Saur, J., Neubauer, F. M., & Glassmeier, K.-H. (2010). Induced magnetic fields in Solar System bodies. *Space Science Reviews*, *152*(1), 391–421.

Saur, J., Strobel, D., & Neubauer, F. (1998). Interaction of the Jovian magnetosphere with Europa: Constraints on the neutral atmosphere. *Journal of Geophysical Research: Planets*, *103*(E9), 19947–19962.

Saur, J., Strobel, D. F., Neubauer, F. M., & Summers, M. E. (2003). The ion mass loading rate at Io. *Icarus*, *163*(2), 456–468.

Schilling, N., Neubauer, F., & Saur, J. (2008). Influence of the internally induced magnetic field on the plasma interaction of Europa. *Journal of Geophysical Research: Space Physics*, *113*(A3).

Schilling, N., Neubauer, F. M., & Saur, J. (2007). Time-varying interaction of Europa with the jovian magnetosphere: Constraints on the conductivity of Europa's subsurface ocean. *Icarus*, *192*(1), 41–55.

Schunk, R., & Nagy, A. (2009). *Ionospheres: physics, plasma physics, and chemistry.* Cambridge university press.

Seufert, M., Saur, J., & Neubauer, F. M. (2011). Multi-frequency electromagnetic sounding of the Galilean moons. *Icarus*, *214*(2), 477–494.

Shematovich, V., Johnson, R., Cooper, J., & Wong, M. (2005). Surface-bounded atmosphere of Europa. *Icarus*, *173*(2), 480–498.

Sittler, E., & Strobel, D. (1987). Io plasma torus electrons: Voyager 1. *Journal of Geophysical Research: Space Physics*, *92*(A6), 5741–5762.

Smyth, W., & Marconi, M. L. (2006). Europa's atmosphere, gas tori, and magnetospheric implications. *Icarus*, *181*(2), 510–526.

Spencer, J., Tamppari, L. K., Martin, T. Z., & Travis, L. D. (1999). Temperatures on Europa from Galileo photopolarimeter-radiometer: nighttime thermal anomalies. *Science*, *284*(5419), 1514–1516.

Stone, J., & Norman, M. L. (1992a). ZEUS-2D: A radiation magnetohydrodynamics code for astrophysical flows in two space dimensions. II. The magnetohydrodynamic algorithms and tests. *The Astrophysical Journal Supplement Series*, *80*, 791–798.

Stone, J., & Norman, M. L. (1992b). ZEUS-2D: A radiation magnetohydrodynamics code for astrophysical flows in two space dimensions. I. The hydrodynamic algorithms and tests. *The Astrophysical Journal Supplement Series*, *80*, 753–790.

Teolis, B., Wyrick, D., Bouquet, A., Magee, B., & Waite, J. (2017). Plume and surface feature structure and compositional effects on Europa's global exosphere: Preliminary Europa mission predictions. *Icarus*, *284*, 18–29.

Vorburger, A., & Wurz, P. (2018). Europa's ice-related atmosphere: the sputter contribution. *Icarus*, *311*, 135–145.